Neutron imaging of operando proton exchange membrane fuel cell with novel membrane

Jongmin Lee, Huu-Dat Nguyen, Sylvie Escribano, Fabrice Micoud, Sebastien Rosini, Alessandro Tengattini, Duncan Atkins, Gérard Gebel, Cristina Iojoiu, Sandrine Lyonnard, et al.

Version of Record: https://www.sciencedirect.com/science/article/pii/S037877532100375X
Manuscript_904a4c9648d2768f44d602bb311fedd5

Neutron imaging of operando proton exchange membrane fuel cell with novel membrane

Jongmin Lee[1], Huu-Dat Nguyen[2], Sylvie Escribano[1], Fabrice Micoud[1], Sebastien Rosini[1], Alessandro Tengattini[3], Duncan Atkins[3], Gérard Gebel[1], Cristina Iojoiu[2], Sandrine Lyonnard[4], Arnaud Morin[1*]

[1]Univ. Grenoble Alpes, CEA, LITEN, F-38000 Grenoble, France
[2] Univ. Grenoble Alpes, Univ. Savoie Mont Blanc, CNRS, Grenoble INP, LEPMI, F-38000 Grenoble, France
[3]Institut Laue-Langevin, F-38042 Grenoble Cedex 9, France
[4] Univ. Grenoble Alpes, CEA, CNRS, IRIG, SyMMES, F-38054 Grenoble, France

Keywords

Polymer electrolyte membrane fuel cell, alternative membrane, neutron imaging, water distribution

***Corresponding author:**

E-mail address: arnaud.morin@cea.fr

Abstract

The performance of an alternative membrane based on aromatic multiblock copolymer was compared to that of the conventional perfluorosulfonic acid (PFSA) polymer membrane during fuel cell operation. The fuel cell with the alternative membrane exhibited more severe voltage loss than the conventional at current densities above 0.6 A/cm^2 with fully saturated reactants. To rationalize this difference, operando high-resolution neutron imaging was used to investigate water distribution in the fuel cells, in parallel with impedance measurements. The type of membrane strongly affected water distribution, not only from anode to cathode, but also in-plane between ribs and channels. Specifically, in the alternative membrane, ionomer in cathode catalyst layer was less hydrated and dried as current density increased. The voltage loss with the alternative membrane was ascribed to ionomer drying rather than to the accumulation of liquid water, in accordance with the evolution of ohmic resistance. Furthermore, the alternative membrane experienced swell/shrinkage resulting in material shifts during the operation. These results pinpoint that developing new ionomers for fuel cells require not only to quantify the bulk transport properties of alternative membranes compared to PFSA, but also to evaluate their interfacial properties and the impact of ionomer on water management.

1. Introduction

A low temperature polymer electrolyte membrane fuel cell (PEMFC) is a clean energy conversion device that is expected to play a significant role in electrifying transportation systems [1]. The PEMFC generates electricity through the electrochemical reactions of hydrogen oxidation and oxygen reduction, producing water as the only by-product. Compared to electric vehicles powered by batteries, fuel cell vehicles offer the promise of a longer driving range and much faster charging time [2,3]. The core of the PEMFC is the membrane electrode assembly (MEA) composed of a proton-conducting polymer membrane, catalyst layers (CLs), and gas diffusion layers (GDLs), clamped between a pair of bipolar plates (flow fields for reactant gases and coolants). The performance and the lifetime of the PEMFC are mostly governed by the characteristics of the materials employed in the various components. Therefore, significant efforts were dedicated to develop novel materials for performance improvement and cost reduction, with an emphasis on the MEA where electrochemical conversion takes place.

In the low temperature PEMFC, the ionomer membrane, located at the centre of the MEA, plays a central role in the performance. It electronically insulates the anode and the cathode and prevents reactants crossover. On the other hand, the protons (H^+) produced at the anode must be conducted through the membrane to the cathode. Therefore, the membrane must be thin for reduced proton resistance, while maintaining good chemical and mechanical stabilities. Among solid polymer electrolytes satisfying these constraints, perfluorosulfonic acid (PFSA) ionomer has become the most successful [4]. The PFSA is composed of a copolymer: a polytetrafluoroethylene (PTFE) backbone and perfluorinated vinylether side chains ending with a sulfonic acid group. The PTFE backbone provides chemical, mechanical stabilities, and hydrophobicity to the polymer, while the sulfonic acid groups render

hydrophilicity. When the sulfonic acid groups are hydrated, continuous pathways for proton conduction are created along the hydrophilic water phase of PFSA ionomer. The first PFSA membrane, known as Nafion®, was developed in 1960s by DuPont [5]. Up to the date, PFSA is still the most commonly used type of polymer due to its high proton conductivity and chemical stability. However, its high cost impedes the commercialisation of PEMFC systems [6,7], and the complex synthesis process of the ionomer limits research developments to a small number of laboratories [7].

Various types of solid electrolyte membranes have been developed as alternatives to the PFSA materials in low temperature PEMFC [8,9]. Recently, Nguyen et al. [7,10,11] introduced a novel performing membrane based on poly (arylene ether sulfone) multiblock copolymers containing perfluorosulfonated side chains as in PFSA ionomer. The chemical structure of this copolymer is shown in Figure 1. The aromatic copolymer features a well-defined hydrophilic/hydrophobic phase-separation, high proton conductivity, low gas permeability (reduced gas cross-over), and superior mechanical properties compared to the PFSA ionomer [12,13]. Various lengths of the hydrophilic and hydrophobic backbone segments were tested with the conclusion that 15000 g/mol of each (hence its common name "In1515") was optimal for PEMFC applications. The performance of In1515 in fuel cells has been evaluated by electrochemical techniques. When In1515 was incorporated in both the CL and the membrane, the PEMFC exhibited similar power output to that obtained using Nafion [7]. However, it is still unknown how the alternative membrane behaves in terms of water management.

Generally, all physical and chemical phenomena in the PEMFC depend on the local water concentration in the sub-components. The membrane plays a crucial role in both through-

plane and in-plane water distribution, by balancing the water content between anode and cathode via two main mechanisms, i.e. diffusion due to gradient of chemical activity and electro-osmosis induced by gradient of electric potential. These phenomena depend primarily on the intrinsic transport properties of the ionomer. Furthermore, the accumulation of water affect the physical and the transport properties of the membrane, which impose a challenge in understanding the phenomena. As discussed in the literature [14–18], the difference in performance between the alternative ionomer and the conventional PFSA is not only attributed to the membrane ionic conductivities, but also to the interaction between the membrane and the CL [19,20] and distinct membrane/CL swelling properties causing a discontinuity in ionic conductivity [21]. The performance of PEMFC with alternative membranes has not yet been analysed by taking account for the impact of the water distribution and transport properties in the other components. Hence, in situ diagnostic of liquid water distribution is highly valuable for further understanding and improving the performance of the alternative membrane.

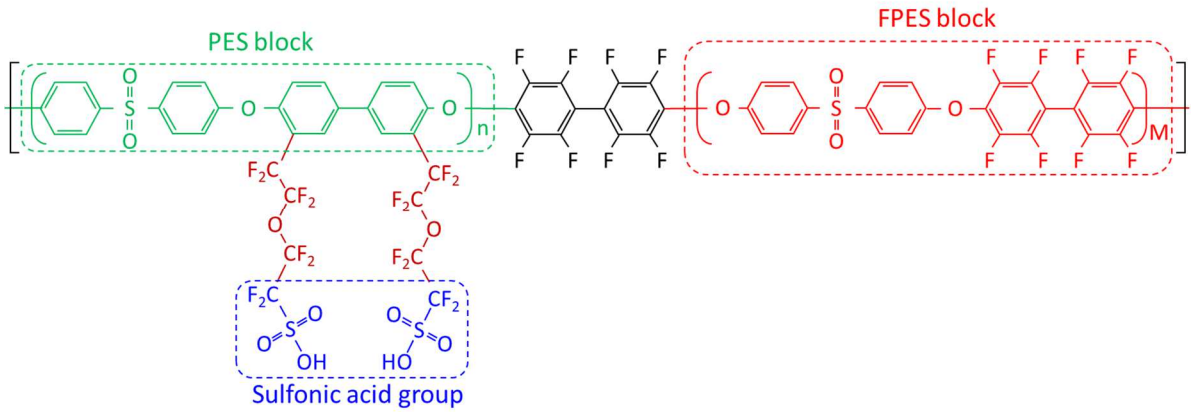

Figure 1. Structure of partially fluorinated multiblock copoly (ether sulfone) bearing polyfluorosulfonic functions (ion exchange capacity (IEC) equals to 1.3 mmol/g. In1515 refers to an ionomer with the length of backbone of hydrophilic (PES) and hydrophobic

(FPES) segments = 15000 g/mol and 15000 g/mol. Two perfluorosulfonic acids were on the grafted/structural unit of hydrophilic block.

Imaging techniques have made significant contributions to material developments and to the understanding of transport phenomena in PEFMC, from identifying water distribution in the flow fields [22] to defining water clusters and their connectivity in the GDLs [23] and membrane [24]. Particularly, neutron and x-ray synchrotron sources produce high intensity beams that enable high spatial and temporal resolutions essential for discerning microstructural changes and water distribution in the MEA of an operating PEMFC [24–30]. Neutron imaging produces a strong signal contrast for water due to relatively large absorption cross-section of hydrogen, which makes it an optimal tool for characterising the water distribution in the membrane and the adjacent porous layers. Recently, significant improvements have been made in high-resolution neutron imaging (from the order of 10-100 to few μm per pixel in few seconds), by means including anisotropic setups [25] and improved detector [31]. In-plane neutron imaging of PEMFC can provide the water profile across the MEA, from which the influence on water distribution of bulk membrane or membrane/CL interfacial transport properties can be elucidated. Therefore, the use of this technique is highly valuable to the investigation of alternative membranes.

In this work, we report on the water distribution in both conventional and alternative MEAs used for operating PEMFC under various humidity levels using high-resolution in-plane neutron radiography. Simultaneously to in situ neutron radiography data acquisition, the fuel cells were characterized electrochemically to determine the proton conductivity and overall performance. We clarify the differences in PEMFC performance by analysing the mean water

content and the heterogeneous water distribution across the various components, under ribs and channels, and their dependence on membrane design.

2. Methodology

2.1 Fuel cell setup and operation

The MEA was prepared in-house. To fabricate In1515 membrane, the precursor containing hydrophilic (PES) and hydrophobic blocks (FPES) in a 7 wt.% Li^+ in dimethyl sulfoxide (DMSO) was casted onto a glass substrate with a knife film applicator. After evaporating solvent at 60°C, the membrane was thermally annealed at 150°C for 24 hrs in a vacuum chamber. Finally, the membrane was treated in 2M HCl. Further detailed description of In1515 fabrication can be found in our previous works [7,10,11]. The thicknesses of N212 and In1515 membranes were 51 and 70 +/- 3 µm, respectively. The platinum loadings for the cathode and anode CLs were ~0.47 and ~0.22 mg_{pt}/cm^2, respectively. The PFSA-based CLs were coated onto the microporous layer (MPL) of commercial GDL (SGL 28 BC) resulting in the thickness of ~15 µm for cathode and ~10 µm for the anode. A pair of gas diffusion electrodes (GDE), which henceforth annotates for the GDL coated with the CL, was hot-pressed with the membranes at 130°C, 3.5 MPa for 6 min. During hot-pressing a 200-µm-thick Teflon gasket was placed around the active area to pre- compress the GDE. After hot-pressing, the MEA containing a pair of GDE, the membrane, and the gaskets, was placed in the single cell for testing and imaging.

The single cell was customized for through-plane neutron imaging to investigate water distribution across the MEA (i.e. beam is parallel to the plane of PEMFC). The endplates were made of low neutron absorption aluminum, coated with gold for better electrical contact and corrosion resistance. The length of the channel was 12 mm so as to limit the width of the

cell and consequently the length of the path of neutrons in the sample. This single cell features single serpentine channels (channel width: 1mm, channel depth: 0.5 mm, and rib width: 0.8 mm) engraved directly on the endplates that also act as current collectors. The active area of the single cell was 2 cm^2.

The temperature of the single cell was maintained at 80 °C by four sheet-type heaters. Each heater had its own thermocouple and was individually regulated. Electrical load, reactant gases, and exhaust gases were regulated using a commercial Bio-Logic test bench [32,33]. The single cell was operated under galvanostatic mode in which the current density was increased from 0 to 1.4 A/cm^2 in steps to obtain the polarization curve. At each current density, the electrochemical impedance spectroscopy was performed after 3 min of voltage stabilization to monitor the ohmic resistance of the cell during the experiment. The ohmic resistance was measured at high frequencies of either 4 or 20 kHz. These two frequencies were chosen so that the value of the imaginary part of the impedance is very close to zero, and consequently the recoded modulus of the impedance is a good approximation of the ohmic resistance. This protocol was performed with both reactants, H_2/Air, at 50, 80, and 100% relative humidity (RH) for the two cells. The reactant flows for anode and cathode were fixed at 120 and 300 Nml/min, respectively, at 1.5 bar absolute. The corresponding stoichiometric ratios at 1.4 A/cm^2 were 7.1 and 7.5 for anode and cathode. The operation of the single cells at high stoichiometric ratios was necessary to achieve uniform operating conditions along flow channels (i.e. the consumption of reactant gases and the production of water are considered negligible). The concentrations of reactants and products are very close at the inlet and at the outlet, reducing heterogeneity of operation along the flow field. The water distribution in the individual channel and rib is shown in the supplementary information (Figure S2). Because of the high stoichiometry, the velocity of gas in the channel

reaches several m/s that is value close to the those in cell of a stack making these measurements representative of a local conditions in a real stack, for instance close to the air and H_2 inlets [27]. This type of single cell operation is reported as differential cell in the literature[34].

2.2 Neutron imaging data acquisition and processing

Neutron imaging was performed on the D50 (NeXT-Grenoble) instrument at the Institut Laue-Langevin (ILL). The attenuated neutron beam was monitored by the detection system that includes a 5-µm-thick Gd scintillator (neutron to photon), 45° optical mirror and digital camera with an optimised optical equipment. The field of view was 17 mm × 17 mm, and the pixel resolution was 8 µm/pixel. For this imaging setup and our custom single cell, a temporal resolution of 10s per frame was chosen for adequate noise-to-signal ratio. After removing oversaturated pixels due to gamma ray, a Gaussian filter was applied to the raw images in order to smooth out.

The water thickness, $t(x, y, n)$, was calculated by the Beer-Lambert law modified as follows:

$$I(x, y, n) = I_0(x, y)e^{-\mu t(x,y,n)}, \quad (1)$$

where I is the measured beam intensity at pixel position (x, y) for frame number n, I_0 is the intensity of the corresponding pixel at a reference state, and μ is the attenuation coefficient of water in cm^{-1}. To obtain reference state, the cell was dried with excess dry nitrogen gas flows for ~15 min, until the measured cell ohmic resistance reached several tens of Ohm.cm², corresponding to conductivity lower than 10^{-5} S/cm and hydration number (number of water molecules per ionic group) λ lower than 2. All acquisitions were aligned rotationally and

translationally with respect to the reference image prior to the application of Beer-Lambert law.

The Beer-Lambert law assumes a constant value of μ which is found to be case up to a defined thickness of water. Besides, it is critical to determine μ, specific to a beamline as its value is dependent on the distribution of neutron wavelength. Stavropoulou et al. [35] experimentally measured absorption in water at the D50 cold neutron beamline to determine the attenuation coefficient of water. The fitted value of μ was 3.10 cm^{-1} for the water quantity up to 3 mm, above which adjusting factors for phenomena such as neutron scattering must be accounted for. In our investigation, the water content of the MEA in the field of view we examined did not exceed 3 mm.

Figure 2 shows a series of representative processed neutron radiographs where water content in each pixel was quantified. The average water at each y position, $\tilde{t}(y)$, is calculated according to the following equation [36]:

$$\tilde{t}(y) = \frac{1}{N_x N_n} \sum_{i=1}^{N_x} \sum_{j=1}^{N_n} t(x_i, y, n_j), \tag{2}$$

where N_x is the number of pixels in X-directions, and N_n is the number of acquisitions. To obtain $\tilde{t}(y)$ for each current density regime, five acquisitions obtained towards the end of each current density step were averaged after the removal of the background. Processing was carried out using ImageJ, an open source software.

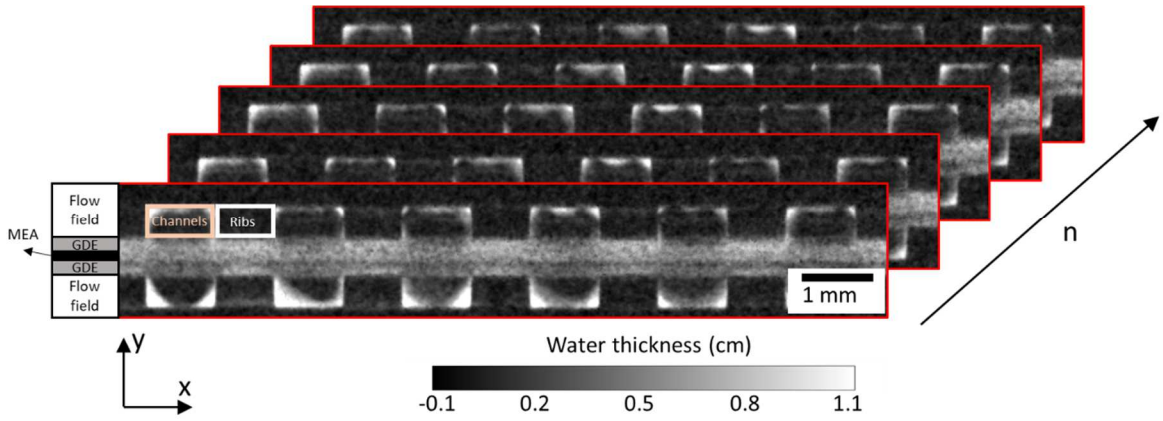

Figure 2. A series of processed neutron radiographs of the single cell showing the various elements (flow field pattern and MEA, y-axis) from inlet to outlet (x-axis), and the levels of water thickness (grey scale) in each pixel as determined from Beer-Lambert law. Mean water profiles are obtained by averaging "n" images during operando measurements.

2.3 Water uptake in the membrane and conductivity

For quantification of the averaged water uptake by the membrane at any time of the operando measurement, the mean water thickness was extracted by analysing the membrane region of the profile (averaged over full x-scale, and y-scale over 7 and 9 pixels for N212 and In1515, respectively). The mean water thickness was converted to volume by multiplying it by the area of single pixel (8 µm × 8 µm), and the corresponding number of moles is then calculated. The water uptake is quantified by the local hydration number, λ, defined as below [37]:

$$\lambda = \frac{n_w}{IEC \times m_m}, \tag{3}$$

where n_w [mol] is the number of moles of water absorbed by the membrane, IEC [mmol/g] is the ionic exchange capacity, and m_m [g] is the mass of membrane. It must be noted that

complete removal of water in the dry (reference state) membrane is not feasible, because it requires vacuum at elevated temperature for an extended period. As a result, in situ neutron imaging has a tendency to underestimate the water uptake in the membrane [38]. In this work, the membrane water content was corrected to compensate for any dimensional changes of the membrane due to the swelling. In future works, efforts will be dedicated to scrutinizing other possible sources of errors in the membrane water measurement such as those described by Hussey et al [38].

The conductivity of the membrane, σ [S/cm], was calculated as follows:

$$\sigma = \frac{L}{R_m \times A}, \tag{4}$$

where L [cm] is the thickness of the membrane (or distance separation between two electrodes), R_m [Ω or 1/S] is the membrane resistance (defined as $R_{total} + R_{elec}$, the sum of the measured resistance and the electronic resistance of the cell with the GDE measured independently, ~ 4 mOhm), and A [cm^2] is the area of the membrane in contact with GDEs (2 cm^2).

3. Results and discussion

3.1 Polarization curve and ohmic resistance

The performance of both cells were evaluated by measuring the IR-compensated voltage (e.g. measured voltage corrected from ohmic drop - see Figure S1 for the uncorrected) and the ohmic resistance at 50%, 80% and 100% RH, for current densities ranging from 0 to 1.4 A/cm^2 (Figure 3). Since the voltage values shown in Figure 3 were corrected for ohmic drop,

the voltage variations (closed symbols) mostly arise from the electrode performance, especially in the cathode considering that the kinetics of hydrogen oxidation reaction (HOR) is much faster than oxygen reduction reaction (ORR), and that H_2 can access more easily to catalytic sites compared to O_2. The ohmic resistance of the cell is usually composed of the bulk resistances of individual components (e.g. membrane, GDE, and current collector) and the contact resistances between them. Here, for the investigation of the two types of membranes, the identical single cell hardware was utilized with the GDEs harvested from the same batch, such that the ohmic resistance difference between cells (Figure 3, open symbols) indeed stems only from the membrane. Thus, the change in the ohmic resistance during the fuel cell operation is only attributed to the hydration level of the membrane (i.e. ionic resistance), which is influenced by, typically, local RH or liquid water accumulation in the GDL and/or CL. Both phenomena usually result in oxygen starvation in the cathode, and the dry-out of ionomer that significantly reduces the utilization of platinum in the electrodes and/or the oxygen reduction reaction kinetics of Pt catalyst [39], therefore reducing fuel cell performance.

The comparison between Nafion and alternative membrane in Figure 3 allows to highlight common features as well as distinct behaviors. The OCV were relative low (~0.9V) possibly due to minor shortcuts between electrodes, but it should not have high impact on the electrochemical nor imaging results for the tested current range (> 0.1 A/cm^2), as no significant cross-over was observed. For both cells, the best performance was obtained at 80% RH (red symbols). At 50% RH (black symbols), the cells exhibited lower performance at all current densities due to ionomer dehydration both in the membrane and in the electrodes. A raw idea of the averaged water content in the membrane can arise from the value of the ohmic resistance (Figure 3). As seen in Figure 3, the ohmic resistances of the

cells decreased with increasing RH levels (due to membrane hydration), and vice versa (due to membrane dehydration). For both cells at 50% RH, the ohmic resistances were reduced significantly as current density increased, which was induced by better hydration of the membrane, due to increased water production and decrease in stoichiometry with fixed gas flows [40]. Indeed, because the inlet gas flows are kept constant, the overall fraction of water in the cell increases with current density.

At 100% RH, the performance was similar to that of 80% RH at low current density, but voltage drops were observed at higher current density, indicating a degraded function of the cathode. This is ascribed to the operation in differential cell at 100%RH on both sides that can promote water accumulation in the gas diffusion layer and in the catalyst layer. However, the non-linear voltage drops occurred more severely at lower current densities in the IN1515 cell compared to the reference Nafion (> 0.6 A/cm^2 for N212 and > 0.4 A/cm^2 for In1515). This loss in performance may arise from increased water accumulation in the active layers and/or GDL (preventing oxygen diffusion), channel and/or ionomer dry-out at the cathode (due to elevated temperature), which are known to be the main causes of non-linear voltage drop. These phenomena are closely related to the water content in the membrane and must be accompanied by evolution of the ohmic resistance with a decrease as local RH increases or an increase in case of drying-out [41,42]. Indeed, the ohmic resistance is larger at 50% RH than for larger RH, as expected. Nonetheless, the ohmic resistance of In1515 showed only a modest increase (9.5 %) from 0.6 to 1.2 A/cm^2 at 100% RH, while it is nearly constant for Nafion. These results do not strongly support any of these two scenarios. In other words, the voltage drop cannot be attributed unambiguously to one of these causes and might even relate to other phenomena such as contact losses between the electrode and the membrane. Clearly, a more detailed investigation is needed to identify the reasons why In1515 is behaving worse

than Nafion in the present conditions, for which operando neutron imaging can provided a significant insight.

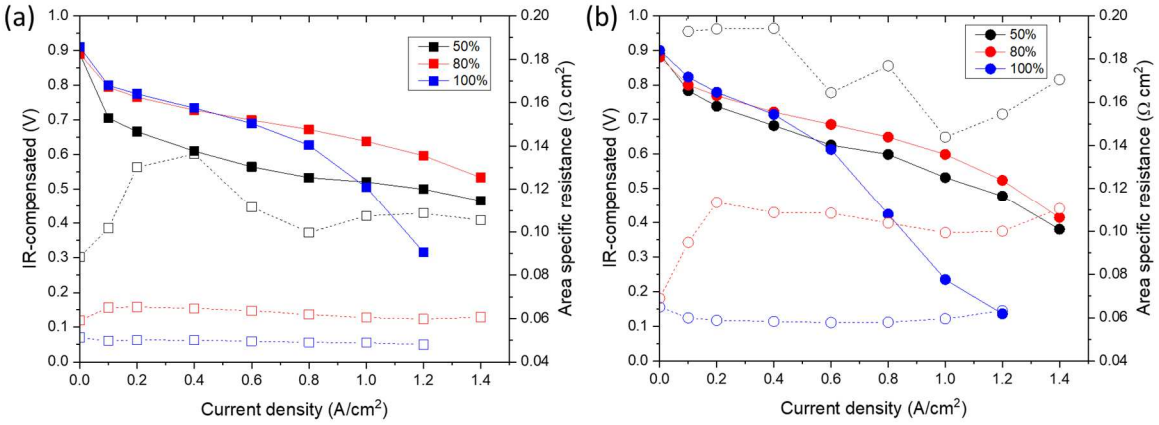

Figure 3. Polarization curves based on IR-compensated voltage (solid markers and lines) and ohmic resistance (empty markers and dotted lines) of the single cells with (a) N212 (square markers) and (b) In1515 (circle markers).

The ohmic resistance data in Figure 3 provide additional information on the distinct behavior of In1515 with respect to Nafion. Indeed, in general the resistances of the cell with In1515 were consistently higher than those of N212, for all humidity levels and current densities. The resistance of the membrane is proportional to its thickness, thus the resistance of In1515 is expected to be higher than that of N212, given that sulfonated acid groups renders similar water absorption behaviour in the both types of membranes [11]. However, as shown in Figure 3 the resistance difference between two cells was greater than a factor of 1.4, i.e. the thickness ratio between In1515 and N212. This implies that N212 facilitated proton transport effectively compared to In1515, which could indicate better hydration, higher conductivity at a given water content, more favorable proton resistance at material interfaces, or a combination of these. The In1515 bulk membrane was reported to be very similar to Nafion

in terms of structure-transport relationship, as due to similar nanoscale ionic structures and same local water-host interactions piloted by perfluorinated side-chain and terminating acidic moiety. In fact, the nanoscale swelling laws are identical, and both the mean size of ionic domains and the bulk proton conductivities show similar values at a given hydration number, λ. The distinct behavior of these two materials during fuel cell operation, therefore, cannot arise from significantly different bulk-ionomer properties, but must rather originate from their efficiency when assembled into MEAs and tested at the device level.

3.2 Membrane water content

The mean membrane water thickness was obtained from the neutron images by integrating the water thickness values in the active area from inlet to outlet, without accounting for the rib/channel pattern at this stage, to analyse the spatially-averaged membrane water content evolution during the operando measurements. The results are shown in Figure 4 as a function of current density (bottom X-axis) and time (top X-axis) for Nafion (a) and In1515 (b). As expected from the resistance measurements, the overall water quantities in N212 were greater than those of In1515 for all conditions. Considering the 40% larger IEC of In1515 compared to Nafion and the similar dependence of the local hydration number as a function of RH for both membranes, one would expect larger water volume fraction in In1515 compared to Nafion, if the average RH in the cell is the same in both tests. For 50 and 80% RH levels, the membrane water content moderately increases with current density, as expected when operating the fuel cell at constant inlet gas flows, as already mentioned above. Indeed, in these conditions, increasing current density results in a higher rate of water production accompanied by diminished water removal. The difference in the mean membrane water contents between two RH levels was rather uniform throughout all current densities, which was also observed in the voltage difference in Figure 3. However, at 100% RH, the cells exhibited different behaviours from those under partially saturated conditions, i.e. a non-

monotonous mean water profiles showing a maximum membrane hydration at intermediate current densities. While the trend is moderate with Nafion (filled blue squares), where the resistance was uniform throughout all current densities (empty blue squares), it is clearly amplified in the case of In1515 fuel cell (blue filled circles), where the mean membrane water content increased before reaching 0.4 A/cm² and decreased above 0.8 A/cm^2, which contributed to small ohmic resistance increase at 1.0 and 1.2 A/cm^2 (blue empty circles). Usually, the operation of fuel cells at high current densities increases the rate of heat production in the CLs (primarily in cathode). This would elevate the local temperature of the adjacent components as well as CLs, which consequently reduces water content in the cell. But, the total membrane water contents of the In1515 fuel cell at the beginning and the end of the operation (0.1 and 1.2 A/cm^2, respectively) were similar regardless of its increase/decrease in between. Still, the increase in the ohmic resistance was shown, which evidences that re-distribution of water content in the fuel cell and/or material changes occurred at high current densities in the In1515 fuel cell. At this point, spatially resolving the distribution of water across the various components and at the rib/channel scale is required to evaluate these hypotheses and provide insights into the origin of the mean water profiles found in the In1515 membrane, which indeed directly correlates to the significant voltage losses at high current densities (> 0.8 A/cm^2) in the IR-corrected polarization curve of In1515 fuel cell.

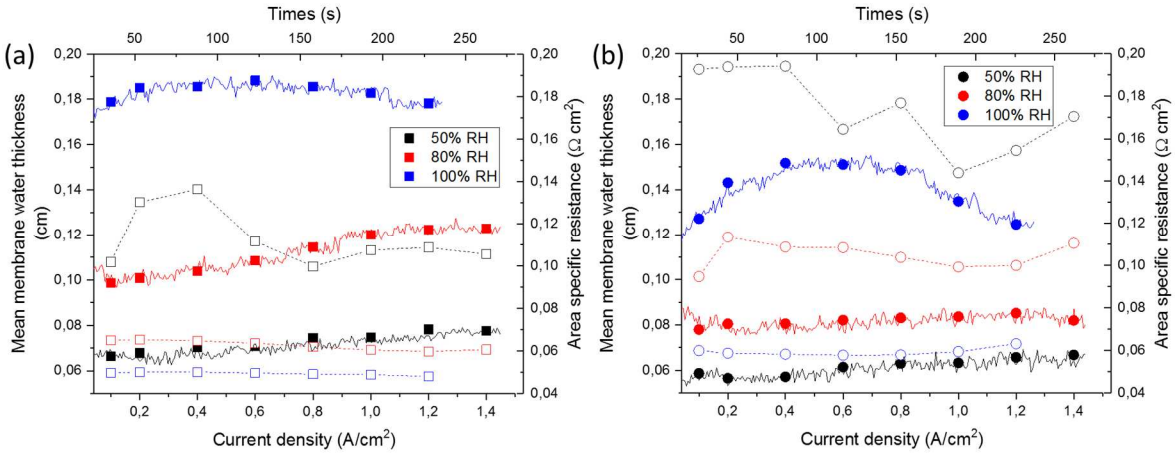

Figure 4. Mean membrane water thickness over time (solid marker and line, left Y-axis) and area specific resistance (empty marker and dotted, right Y-axis) for the fuel cell vs. time (top X-axis) and current densities (bottom X-axis) with (a) N212 and (b) In1515 at 50%, 80%, and 100% RH.

3.3 Rib/channel water content in membrane and GDEs

The analysis of the evolution of the ohmic resistance and mean membrane water content with current density suggests that the voltage loss for N212 fuel cell at 100%RH could be attributed to the water accumulation. But, it is less straightforward for In1515 fuel cell as its ohmic resistance increases while water content decreases as the current is increased. For further analysis and to better understand these evolutions, we need to examine the individual components (cathode/anode GDE and membrane) and to consider separately the water content under the channel and the ribs. It is well established that, water vapour diffused through the GDE tends to condense in the regions near the ribs, because the temperature under the ribs is lower than that under the channel due to cooling. Besides, the water removal through diffusion and convection is more effective in the channel than in the rib; therefore, high amount of liquid water generally accumulates in near the ribs. In Figure 5, we report the average water thickness measured in the cathode GDE (a), the membrane (b), and the anode GDE (c) under ribs (filled symbols) and channels (empty symbols) for Nafion (squared

symbols) and In1515 (round symbols) at 100%RH. The corresponding in-plane (for GDEs and membrane) and through-plane profiles are provided in the supplementary Figure S2 and S3. First of all, we notice that the usual rib/channel effects are clearly shown for anode and cathode GDEs for both fuel cells, in which higher water quantity was systematically observed under the rib regions, as expected. This rib/channel heterogeneity was also found in the membrane, although much less pronounced, in particular in In1515 where the absolute rib/channel difference in water content is < 5% over the full range of current densities, against ~10% in Nafion, pointing, again, to the distinctive water management in the In1515 fuel cell. The most striking observation from Figure 5 is the non-symmetrical situation of anodes and cathodes when comparing the two systems. Indeed, water content in the membrane and the cathode GDE was greater in N212 cell than those in In1515 cell for all current densities[1]. In addition, at high current densities (0.8 to 1.2 A/cm^2), both fuel cells exhibited decreases in the cathode GDE (and the membrane) water contents, as expected from the previous discussion associated to heat production in the CL. However, contrasting behaviours in water content was observed in the anode GDEs of two fuel cells. The water content in the anode GDE of the In1515 cell showed significant decrease as opposed to the increase in the N212 cell.

The voltage of the In1515 fuel cell was lower than that of the N212 fuel cell leading to higher rate of heat production at the given current density, which could be responsible for lower water content in the cathode GDE and the membrane of the In1515 cell. Heat produced would favor evaporation from cathode CL to cathode channel. Nevertheless, the water content reduction in the anode GDE of In1515 fuel cell was rather unusual. For instance,

[1] Note that the average water volume fraction in the pores of GDL never exceeds 30% considering the length of the beam path in the direction of the flow field and taking into account an average porosity about 65% for the compressed GDL with microporous layer. See reference [32] for details on the calculations. This value is in accordance to what has been previously reported in the literature.

during fuel cell operation heat is primarily produced in the cathode CL, and it is unlikely that the impact of heat could manifest significantly only on the anode side. Besides, such predominant reduction in water content at high current density was shown only for the anode GDE of In1515 among all profiles. This shows that the anode/cathode water distribution is dependent on the type of membrane, due to difference in overall water transport properties. The reduction in the anode GDE water may be suspected to be due either to intrinsic bulk or interfacial water transport properties of the membrane or, to poor transfer interface between membrane and CL which could prevent water transfer from cathode to anode in the case of In1515 in comparison with N212. However, this cannot be established using the averaged values presented in this section, as they do not contain any information on where the water molecules are localized in the depth of the various layers.

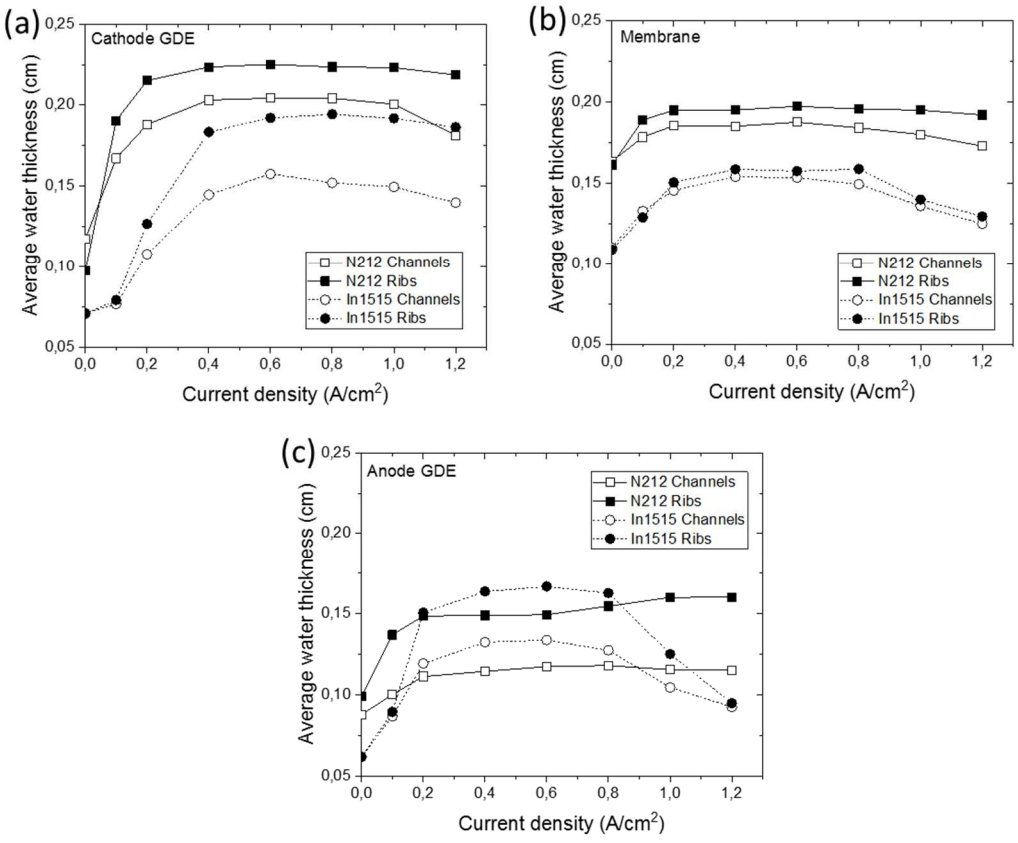

Figure 5. Average water content under the rib (solid marker) and channel (empty marker) regions for (a) cathode GDE, (b) membrane, and (c) anode GDE of the N212 (square marker, solid line) and the In1515 (circle marker, dotted line) fuel cells under 100% RH.

3.4 Water distribution across MEAs

To discern the water distribution across the various elements of the operating fuel cells, we extracted the cross-sectional water profiles, e.g. water thickness across the MEAs (Figure 6). The radiographs of two cells at 0.2, 0.6, and 1.2 A/cm^2 are displayed in Figure 7. For more detailed profiles (e.g. rib/channel, inlet to the outlet), readers may refer to supplementary Figure S2 and S3. Each plot is classified into three sub-regions with respect to the position: cathode GDE, membrane, and anode GDE. The boundary between the GDEs and the membrane corresponds to the position of the catalyst layers (2-3 pixels). The data obtained at 50%, 80% and 100% RH for Nafion and In1515 fuel cells at different current densities (from 0 to 1.2 A/cm^2) are shown on panels (a,b), (c,d) and (e,f), respectively. From this full set of data, few general observations can be qualitatively made: i) the water distribution within each elementary layer is heterogeneous, revealing gradients in water concentration everywhere under all conditions, ii) the water distribution among the GDEs and membrane layers depends on both the humidity and current densities, iii) the higher the humidity, the greater the variations in concentration gradients and absolute water contents in function of the current, and iv) the higher the current density, the greater the heterogeneities between anode and cathode GDEs. These trends, in particular for the Nafion fuel cell behavior, are in agreement with the literature and our expectations, where basically cathode flooding is evidenced when increasing humidity and current density, yielding performance loss. Moreover, our data contain invaluable information that highlight the distinct behavior of In1515 fuel cell, which starts at 80% RH and strikingly develops at 100% RH, exhibiting a new dynamic pattern with respect to Nafion. Indeed, at 50% RH (Figure 6a-b), both fuel cells exhibited the similar

quantity of water, symmetrical with the local maxima, which were located in centers of the membranes. The current increment results in only marginal changes in water profiles for both cells, mainly due to high stoichiometry. The partial pressure of water can hardly reach saturated vapor pressure considering the negligible amount of water that is produced compared to the amount injected in the cell via the humidified reactants. At 80% RH, below 1.0 A/cm^2, the two profiles (Figure 6 (c) and (d)) resembled those at 50% RH with a slightly higher water quantity. For the current densities above 1.0 A/cm^2, significant amount of liquid water was detected in both fuel cells, but in different manners. In the N212 fuel cell, the water was observed in the membrane and the cathode GDEs, more precisely in both the CL and the GDL. The highest water content was observed near the center of the membrane, which progressively decreased towards the GDE side adjacent to the flow field. On the other hand, in the In1515 fuel cell, water was found only at the cathode side in the GDL part of the GDE, not in the CL region nor in the membrane. As already discussed using the mean water content values in the previous sections, the overall quantity of water was much higher in the N212 fuel cell than that in the In1515 fuel cell. In Figure 3, the IR-corrected voltage of the In1515 fuel cell was 0.05, 0.08 and 0.13 V lower than that of the N212 fuel cell for 1.0, 1.2 and 1.4 A/cm^2, respectively. Accordingly, the lower electrochemical performance associated with In1515 can be attributed to the impact of the membrane on the performance of the electrode or on the “utilisation” of the electrode, and most probably of the cathode. Obviously, since the water content in the cathode is lower with In1515 than with Nafion, we can exclude any issue with flooding to explain the difference in performance between the two membranes at 80%RH. Depressed performance with In1515 could be caused by a bad physical interface leading to a reduced contact area in between the membrane and the electrode. Another explanation could be the misuse of the catalyst induced by an under hydrated ionomer as shown with the lower water content in the catalyst layer area on the

profiles. This lower hydration in the electrode could be due to the properties of interfaces between the membrane and the CL, the surface/bulk water properties of In1515, and the compatibility between Nafion ionomer in electrode and In1515 membrane.

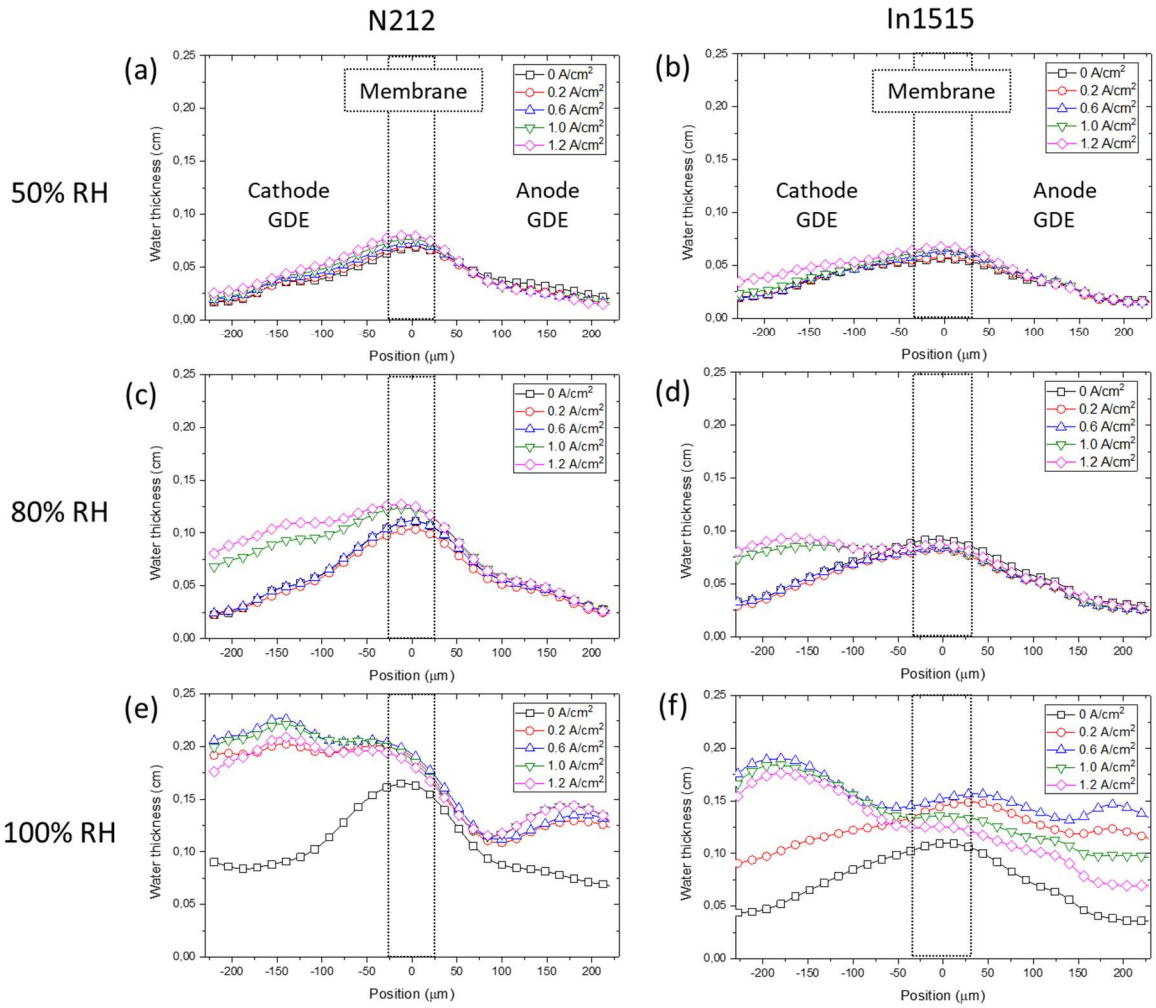

Figure 6. Water thickness profile across the membrane and the GDEs in the fuel cell with: N212 at (a) 50% RH, (c) 80% RH, (e) 100% RH, In1515 at (b) 50% RH, (d) 80% RH, and (f) 100% RH. The dotted boxes indicate the membranes, and the cathode and the anode sides were annotated by negative and positive positions, respectively. The number of data points was here reduced by half (i.e. each marker represents the average of two pixels) to improve visibility of the plot.

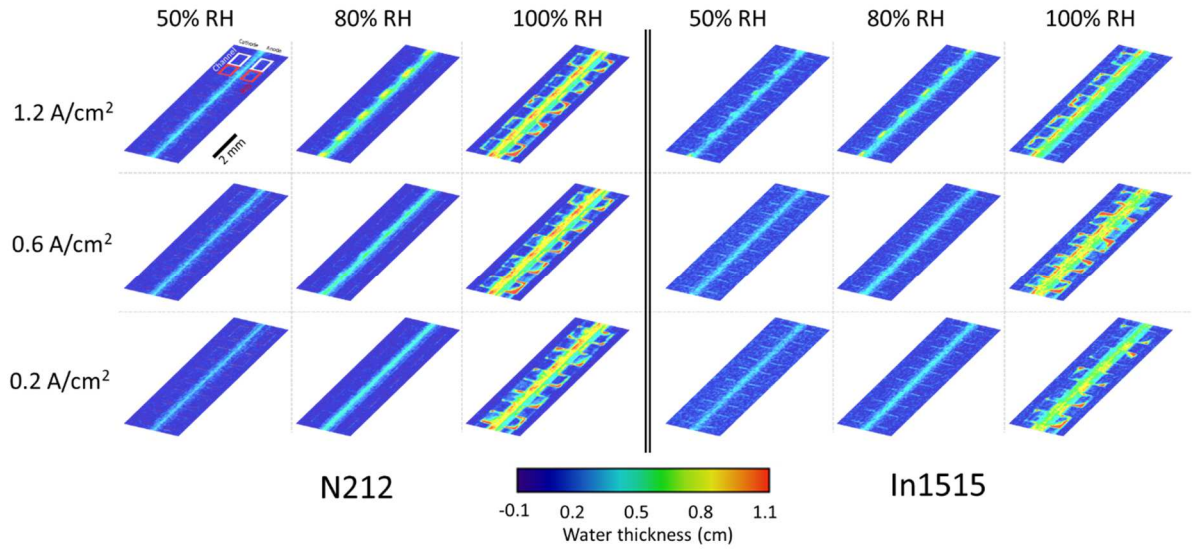

Figure 7. Radiographs of two cells (N212 and In1515) at 0.2, 0.6, and 1.2 A/cm^2 under 50, 80, and 100% RH. The cathode side on the left of the image, and the anode side on the right. Five channels and four ribs at the center are shown.

Under fully humidified conditions, both fuel cells exhibited drastic changes in the water profiles, and three phenomena were observed: (1) water condensation at the open circuit voltage (OCV); (2) water accumulation in the GDE (GDLs and CLs); and (3) water accumulation in/near the membrane. Regarding the first point, at the OCV, noticeably higher water contents were found in all regions, particularly in the membranes (approximately +50% for N212 and +20% for In1515). To achieve 100% RH condition within the fuel cell, the dew points for the gas humidification bubbles were set to 3-5 °C above the temperature of the fuel cells. As the gas flow entered the fuel cell, condensation occurred, and liquid water was detected in the GDL regions even at OCV.

Regarding the second point, e.g. water accumulation in the GDE, we observed that the water content in the CLs (i.e. at the membrane-GDE interfaces) was greater for N212 compared to In1515 at both electrodes. In the CL, water exists by two means: an accumulation in the pores

and as an attachment to the sulfonic acid group of the ionomer. Water accumulation hinders reactant gas transports in the CL causing mass transport loss, whereas water absorption in the ionomer facilitates and improves water transport from the membrane to the catalyst. Unfortunately, it is not possible to distinguish between these two contrasting phenomena with imaging techniques. This requires small angle neutron or X-ray scattering techniques, whereby water absorption in the ionomer is quantified by tracking the position of the ionomer peak that is specific to the hydrophilic-hydrophobic phase separation of the ionomer [33]. Nonetheless, the measurement of combined water content can provide an insight into understanding the mass transport of the fuel cell under flooded conditions. In Figure 3, the polarization curve of the In1515 fuel cell displayed mass transport loss at 100% RH above 0.6 A/cm^2 compared to the N212 fuel cell. Interestingly, despite highest water quantity in the cathode GDE (~ 0.2 cm), and more precisely close to the membrane, N212 fuel cell did not experience as severe mass transport limitations. Accordingly, there is no one-to-one correlation between water content in the GDE, or close to the CL, in the fuel cell and decrease in performance, when comparing the two types of membrane. In conclusion, the low performance of In1515 fuel cell is most probably not due to water accumulation in the cathode GDL but could be attributed to the ionomer dry-out in the cathode electrode, which can be highly localized with uneven heat distribution.

Lastly, regarding point 3, e.g. water accumulation in/near the membrane, we noticed that the two types of membranes behaved differently at 100% RH with current generation. In the N212 fuel cell, water clearly accumulates within the membrane and near the cathode CL on increasing current density, while near the membrane-anode interface there is no significant change. This type of water distribution across the MEA is typical and was previously reported in the literature [43]. In contrast, in the In1515 fuel cell at 100% RH, the local

maximum of water thickness shifted with the increase of current density. For example, the maximum position (initially symmetric around 0 µm at OCV) shifted towards the anode GDE by 5 pixels (40 µm) at 0.6 A/cm^2, where the highest water content was observed.

The shift of the In1515 water profile peak on increasing current density could be due to the distinct bulk/interfacial properties and/or to the displacement of the membrane towards anode due to swelling. Anode-to-cathode water distribution is importantly driven by the membrane water transport properties, namely a balance between self-diffusion and electro-osmosis. The larger anode water content in In1515 fuel cell compared to Nafion fuel cell could in principle be explained by a larger water diffusion coefficient and/or a smaller electroosmotic drag coefficient. However, despite no systematic comparison between In1515 and Nafion bulk water transport properties have been reported, the materials are expected to be close considering the results already published, showing similar proton conductivity and water diffusion coefficient, nanoscale morphologies, and ionization/hydration mechanisms [11–13]. Intrinsic interfacial transport properties might also play a key role and differ from Nafion to the aromatic compound membranes. Higher sorption and lower desorption interfacial transport limitations could lead to larger water contents in the anode for In1515. Beside such intrinsic interfacial transport properties, the application of In1515 membrane onto the Nafion-based ionomer electrode could also cause a discontinuity in transport and water behaviours at the membrane-CL interface. These hypotheses based on bulk or interfacial transport phenomena would deserve proper investigations to be evaluated. In addition, as it has already been shown by Boillat and co-workers [34,44], in differential cell at 100%RH in the anode and cathode channel, the highest water content is expected to be at the cathode side where the water is produced, whatever the bulk or interfacial transport properties of the membrane, and not in the anode GDE. A simpler explanation to the shift of maximum water content observed

in In1515, and not in Nafion, would be a difference in membrane swelling behaviour. Even if the materials are physico-chemically very close, In1515 have sufficiently distinct equivalent weight, density and water sorption capacities, to undergo a larger swelling than Nafion. According to available sorption isotherm data, assuming isotropic behaviour and absence of porosities, the dimensional change is 30 to 40% larger for In1515 compared to Nafion, for which it is about 10% expected. Thus, the maximum water content on the profiles could correspond to the position of the membrane which would move significantly more in the case of In1515 compared to Nafion. The cross-sectional water distribution through neutron imaging is not sufficient to fully confirm the swelling and shrinking of the membrane during the fuel cell operation. But, the material movements (due to membrane swell/shrinkage) within operating fuel cells has have been reported in the literature [45,46]. According to Ge et al. [46], in order to carry out an accurate water measurement in an operando fuel cell, membrane swelling upon hydration must be taken into account as it can lead to non-physical water content measurements, particularly at membrane-CL boundaries. The calculations are made under the assumption that the production of water is the only difference between the reference and the sample images but, for instance, the expansion of the membrane upon hydration results in geometrical changes in the sample. Therefore, the membrane swell region (originally occupied by CL or GDL in the reference) is perceived as water accumulation in the CL or GDL.

3.5 Possible membrane swell/shrinkage and topology map

To further examine the shift toward the anode for In1515, the topology map of MEA centre region (±60 µm) was obtained, as shown in Figure 8. The positions along the flow channel (in the horizontal direction), from the inlet to the outlet, were segmented into 16 regions, 8 channels and 8 ribs, denoted as C_i and R_i, respectively (i=1 to 8). Vertically, the cathode GDE, membrane and the anode GDE are displayed over 120 microns in total, 0 being the

reference position for the membrane. The water content levels are color-coded and shown for Nafion (left) and In1515 (right) fuel cells, from OCV to 1.2 A/cm^2 current density, red being the most hydrated zones and blue the most depleted ones (within each C_i/R_i segment). Qualitatively, it is obvious from these cross-sectional images that the In1515 maps are much fuzzier, in particular at high current density, while the Nafion maps maintain more regular rib/channel and cathode-membrane-anode patterns, where interfaces are better defined. During operation of the N212 cell, it can clearly be seen that the highest water content was observed at the membrane-cathode CL regions. This water gradient within N212 is evident, which remained relatively unchanged for all current densities. In contrast, the maxima of In1515 shifted towards anode until 0.8 A/cm^2 with membrane hydration. It is feasible that the membrane expanded into the anode CL. Beyond 0.8 A/cm^2, the membrane may have shrunk and returned close to its original dimension because of drying that might have been induced by increase in temperature, and the maxima did not display any relationship neither with the distance from the inlet, nor with the outlet and the locations of channels and ribs. It is worth noting that the decay in performance and the shift back of the membrane occurs concomitantly as the current density increases. Therefore, it is tempting to correlate the two phenomena. In-plane membrane swelling could result in surface wrinkles and unevenness, which may explain the peak shift of 40 µm that is greater than expansion in thickness, supposed not to exceed 15-20% of the original thickness of the membrane (15 µm). The distortion of the In1515 would worsen the quality of the contact between membrane and catalyst layer.

As was previously mentioned, for the fabrication of the MEA, the membrane and two GDEs were hot-pressed to improve the CL/membrane interfacial contact. The CL contains Nafion ionomer (33 wt.%) as a proton conducting medium, and which exists as films on the Pt/C

composite and agglomerates [47]. During hot-pressing, PFSA ionomer molecules in the membrane and the CL form a network that is expected to result in a more uniform and stronger interaction at their interface than that formed by In1515 membrane and the PFSA-based CLs. [48–50]. Furthermore, according to Lee et al. [7], storage moduli for Nafion and In1515, measured by dynamic mechanical analysis, are 400 and 1700 MPa, respectively. Storage modulus is a measure for elastic response of a material and stored energy. It implies that the mechanical strength (or rigidity) of In1515 is higher than that of N212. It may be postulated that the relatively soft Nafion membrane underwent a more efficient CL pore impregnation compared to the alternative membrane, thus creating better interfacial contact. The quality of the adhesion along with the lower stiffness would allow limiting the in-plane expansion of the Nafion compared to In1515. They would also keep a better contact in between the membrane and the catalyst layer, and therefore better performance.

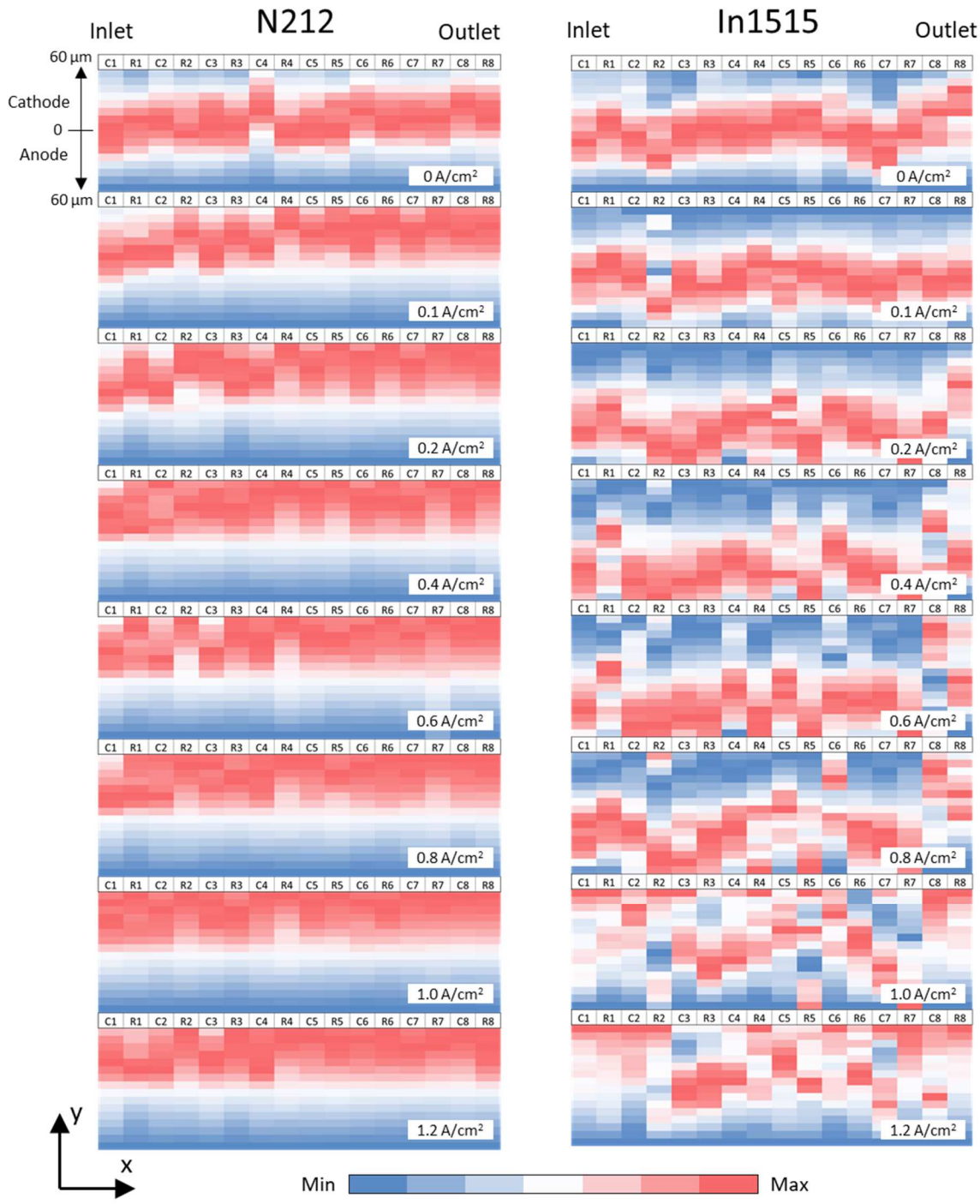

Figure 8. Water topology map of the MEA centre region (±60 µm) with N212 (left) and In1515 (right) for current densities from 0 to 1.2 A/cm^2. The X-positions from the inlet to the outlet were segmented into 8 channels and 8 ribs, represented by C and R, respectively, followed by number. The max and the mean values (within each segment) were assigned as blue and red. White corresponds to 50% percentile within each channel or rib.

4. Conclusions

In this work, the performance of the fuel cell incorporating an alternative membrane In1515, based on poly-multiblock copolymers containing perfluorosulfonated side chains, was compared to that of a fuel cell with conventional PFSA-based membrane, N212. Neutron imaging was employed to study the water content in the MEAs of operating fuel cells, in particular the in-plane and though-place water distribution at the level of the individual components. A significant voltage loss under high current density at 100% RH was observed for the alternative membrane cell, which is usually ascribed to flooding in GDLs/CLs. In contrast, the N212 fuel cell did not display such large mass transport loss, although a higher quantity of water was detected in the GDEs and membrane of the N212 fuel cell for most conditions, compared to the aromatic-based fuel cell. In addition, the In1515 fuel cell exhibited less water content near the cathode catalyst layer region resulting in ionomer dry-out, which could have worsened with current (heat) generation and local effects. These results indicate that decay in performance as current density increases can not always be ascribed to flooding of the GDL and/or catalyst layer. The heterogeneous distribution of water in the alternative fuel cell was modified with respect to the reference one, showing that the In1515 polymer induces a distinct water management in the device, although bearing similar ex-situ structure/transport bulk properties than Nafion. Besides, unexpected peak shift in the water profile occurred near the membrane-anode CL interface. The cause of the shift is not fully identified – multiple phenomena in the fuel cell are coupled, for which reliable physical description is lacking or knowledge of relevant parameters are unknown. However, it was hypothesized that the application of In1515 membrane on PFSA-based CL could induce discontinuities in transport and water behaviours at the interface. This may have resulted in uneven swelling/wrinkle of In1515 membrane, which contributed to the voltage

drop at the high current density. Imaging or tomography experiments with better resolution are required to confirm this hypothesis. Overall, this work emphasises the importance of interfacial engineering to optimize the use of alternative membranes. Ex-situ characterization of bulk materials is usually performed to quantify hydration numbers, diffusion coefficients, transport coefficients, elastic moduli and other key features of a proton-conducting membrane, but they must be complemented by in situ device-level testing to qualify the ability of new polymers to insure efficient water distribution in the system. Particularly, mechanical properties and continuity in ionic conduction and water transport properties (i.e. between ionomer in CL and ionomer in membrane) are critical to optimize the behavior of PFSA-alternative materials for a practical use in fuel cells. In the future works, the water distribution in the various membrane and CL will be quantified to further investigate the effect of CL ionomer-membrane interface, in which all materials will be developed in-house for improved consistency.

Acknowledgement

The CEA-Enhanced Eurotalents program for Dr. Jongmin Lee is acknowledged. The authors thank Institut Carnot Energies du Futur for funding this project and Institut Laue-Langevin for beamtime allocation. The authors thanks to NSPEM project for funding the research on the development of alternative membranes.

References

[1] C. Fiori, A. Dell'Era, F. Zuccari, A. Santiangeli, A. D'Orazio, F. Orecchini, Critical review of fuel cell's membranes and identification of alternative types for automotive applications, Int. J. Hydrog. Energy. 40 (2015) 11949–11959. https://doi.org/10.1016/j.ijhydene.2015.03.105.

[2] C.C. Chan, The State of the Art of Electric, Hybrid, and Fuel Cell Vehicles, Proc. IEEE. 95 (2007) 704–718. https://doi.org/10.1109/JPROC.2007.892489.

[3] O. Gröger, H.A. Gasteiger, J.-P. Suchsland, Review—Electromobility: Batteries or Fuel Cells?, J. Electrochem. Soc. 162 (2015) A2605. https://doi.org/10.1149/2.0211514jes.

[4] B. Smitha, S. Sridhar, A.A. Khan, Solid polymer electrolyte membranes for fuel cell applications—a review, J. Membr. Sci. 259 (2005) 10–26. https://doi.org/10.1016/j.memsci.2005.01.035.

[5] S. Banerjee, D.E. Curtin, Nafion® perfluorinated membranes in fuel cells, J. Fluor. Chem. 125 (2004) 1211–1216. https://doi.org/10.1016/j.jfluchem.2004.05.018.

[6] fcto_cost_analysis_pem_fc_5-10kw_backup_power_0.pdf, (n.d.). https://www.energy.gov/sites/prod/files/2016/12/f34/fcto_cost_analysis_pem_fc_5-10kw_backup_power_0.pdf (accessed December 13, 2018).

[7] H.-F. Lee, M. Killer, B. Britton, Y. Wu, H.-D. Nguyen, C. Iojoiu, S. Holdcroft, Fuel Cell Catalyst Layers and Membrane-Electrode Assemblies Containing Multiblock Poly(arylene ether sulfones) Bearing Perfluorosulfonic Acid Side Chains, J. Electrochem. Soc. 165 (2018) F891–F897. https://doi.org/10.1149/2.1081810jes.

[8] A. Kraytsberg, Y. Ein-Eli, Review of Advanced Materials for Proton Exchange Membrane Fuel Cells, Energy Fuels. 28 (2014) 7303–7330. https://doi.org/10.1021/ef501977k.

[9] D.W. Shin, M.D. Guiver, Y.M. Lee, Hydrocarbon-Based Polymer Electrolyte Membranes: Importance of Morphology on Ion Transport and Membrane Stability, Chem. Rev. 117 (2017) 4759–4805. https://doi.org/10.1021/acs.chemrev.6b00586.

[10] H.-D. Nguyen, L. Assumma, P. Judeinstein, R. Mercier, L. Porcar, J. Jestin, C. Iojoiu, S. Lyonnard, Controlling Microstructure–Transport Interplay in Highly Phase-Separated Perfluorosulfonated Aromatic Multiblock Ionomers via Molecular Architecture Design, ACS Appl. Mater. Interfaces. 9 (2017) 1671–1683. https://doi.org/10.1021/acsami.6b12764.

[11] L. Assumma, C. Iojoiu, R. Mercier, S. Lyonnard, H.D. Nguyen, E. Planes, Synthesis of partially fluorinated poly(arylene ether sulfone) multiblock copolymers bearing perfluorosulfonic functions, J. Polym. Sci. Part Polym. Chem. 53 (2015) 1941–1956. https://doi.org/10.1002/pola.27650.

[12] H.-D. Nguyen, L. Assumma, P. Judeinstein, R. Mercier, L. Porcar, J. Jestin, C. Iojoiu, S. Lyonnard, Controlling Microstructure–Transport Interplay in Highly Phase-Separated Perfluorosulfonated Aromatic Multiblock Ionomers via Molecular Architecture Design, ACS Appl. Mater. Interfaces. 9 (2017) 1671–1683. https://doi.org/10.1021/acsami.6b12764.

[13] L. Assumma, H.-D. Nguyen, C. Iojoiu, S. Lyonnard, R. Mercier, E. Espuche, Effects of Block Length and Membrane Processing Conditions on the Morphology and Properties of

Perfluorosulfonated Poly(arylene ether sulfone) Multiblock Copolymer Membranes for PEMFC, ACS Appl. Mater. Interfaces. 7 (2015) 13808–13820. https://doi.org/10.1021/acsami.5b01835.

[14] A. Guimet, L. Chikh, A. Morin, O. Fichet, Effect of a neutral fluorinated network on the properties of a perfluorosulfonic acid ionomer as proton exchange membrane, Int. J. Hydrog. Energy. 41 (2016) 15562–15572. https://doi.org/10.1016/j.ijhydene.2016.05.240.

[15] A. Guimet, L. Chikh, A. Morin, O. Fichet, Strengthening of perfluorosulfonic acid ionomer with sulfonated hydrocarbon polyelectrolyte for application in medium-temperature fuel cell, J. Membr. Sci. 514 (2016) 358–365. https://doi.org/10.1016/j.memsci.2016.04.031.

[16] V. Delhorbe, S.R. Reijerkerk, C. Cailleteau, M. Bathfield, L. Chikh, F. Gouanve, L. Ogier, E. Espuche, B. Ameduri, S. Vidal, G. Gebel, A. Morin, O. Fichet, Polyelectrolyte/fluorinated polymer interpenetrating polymer networks as fuel cell membrane, J. Membr. Sci. 429 (2013) 168–180. https://doi.org/10.1016/j.memsci.2012.11.032.

[17] P.M. Legrand, A. Morin, V.H. Mareau, L. Gonon, Impact of gas stoichiometry on water management and fuel cell performance of a sulfonated Poly(Ether Ether Ketone) membrane, J. Power Sources. 206 (2012) 161–170. https://doi.org/10.1016/j.jpowsour.2012.01.102.

[18] M.-C. Clochard, T. Berthelot, C. Baudin, N. Betz, E. Balanzat, G. Gébel, A. Morin, Ion track grafting: A way of producing low-cost and highly proton conductive membranes for fuel cell applications, J. Power Sources. 195 (2010) 223–231.

[19] M. Breitwieser, M. Klingele, S. Vierrath, R. Zengerle, S. Thiele, Tailoring the Membrane-Electrode Interface in PEM Fuel Cells: A Review and Perspective on Novel Engineering Approaches, Adv. Energy Mater. 8 (2018) 1701257. https://doi.org/10.1002/aenm.201701257.

[20] S. Vierrath, M. Breitwieser, M. Klingele, B. Britton, S. Holdcroft, R. Zengerle, S. Thiele, The reasons for the high power density of fuel cells fabricated with directly deposited membranes, J. Power Sources. 326 (2016) 170–175. https://doi.org/10.1016/j.jpowsour.2016.06.132.

[21] J. Zhang, H. Zhang, J. Wu, J. Zhang, Chapter 2 - Design and Fabrication of PEM Fuel Cell MEA, Single Cell, and Stack, in: J. Zhang, H. Zhang, J. Wu, J. Zhang (Eds.), Pem Fuel Cell Test. Diagn., Elsevier, Amsterdam, 2013: pp. 43–80. https://doi.org/10.1016/B978-0-444-53688-4.00002-4.

[22] T.A. Trabold, J.P. Owejan, D.L. Jacobson, M. Arif, P.R. Huffman, In situ investigation of water transport in an operating PEM fuel cell using neutron radiography: Part 1 – Experimental method and serpentine flow field results, Int. J. Heat Mass Transf. 49 (2006) 4712–4720. https://doi.org/10.1016/j.ijheatmasstransfer.2006.07.003.

[23] J. Eller, J. Roth, F. Marone, M. Stampanoni, F.N. Büchi, Operando Properties of Gas Diffusion Layers: Saturation and Liquid Permeability, J. Electrochem. Soc. 164 (2017) F115–F126. https://doi.org/10.1149/2.0881702jes.

[24] S. Deabate, G. Gebel, P. Huguet, A. Morin, G. Pourcelly, 3 In situ and operando determination of the water content distribution in proton conducting membranes for fuel cells: a critical review, Energy Environ. Sci. 5 (2012) 8824–8847. https://doi.org/10.1039/C2EE21834H.

[25] P. Boillat, E.H. Lehmann, P. Trtik, M. Cochet, Neutron imaging of fuel cells – Recent trends and future prospects, Curr. Opin. Electrochem. 5 (2017) 3–10. https://doi.org/10.1016/j.coelec.2017.07.012.

[26] S.-G. Kim, S.-J. Lee, A review on experimental evaluation of water management in a polymer electrolyte fuel cell using X-ray imaging technique, J. Power Sources. 230 (2013) 101–108. https://doi.org/10.1016/j.jpowsour.2012.12.030.

[27] R. Mukundan, R.L. Borup, Visualising Liquid Water in PEM Fuel Cells Using Neutron Imaging, Fuel Cells. 9 (2009) 499–505. https://doi.org/10.1002/fuce.200800050.

[28] C. Hartnig, I. Manke, MEASUREMENT METHODS | Structural Properties: Neutron and Synchrotron Imaging, In-Situ for Water Visualization, in: J. Garche (Ed.), Encycl. Electrochem. Power Sources, Elsevier, Amsterdam, 2009: pp. 738–757. https://doi.org/10.1016/B978-044452745-5.00078-2.

[29] A. Bazylak, Liquid water visualization in PEM fuel cells: A review, Int. J. Hydrog. Energy. 34 (2009) 3845–3857. https://doi.org/10.1016/j.ijhydene.2009.02.084.

[30] Q. Meyer, Y. Zeng, C. Zhao, In Situ and Operando Characterization of Proton Exchange Membrane Fuel Cells, Adv. Mater. 31 (2019) 1901900. https://doi.org/10.1002/adma.201901900.

[31] C. Tötzke, I. Manke, A. Hilger, G. Choinka, N. Kardjilov, T. Arlt, H. Markötter, A. Schröder, K. Wippermann, D. Stolten, C. Hartnig, P. Krüger, R. Kuhn, J. Banhart, Large area high resolution neutron imaging detector for fuel cell research, J. Power Sources. 196 (2011) 4631–4637. https://doi.org/10.1016/j.jpowsour.2011.01.049.

[32] N. Martinez, Z. Peng, A. Morin, L. Porcar, G. Gebel, S. Lyonnard, Real time monitoring of water distribution in an operando fuel cell during transient states, J. Power Sources. 365 (2017) 230–234. https://doi.org/10.1016/j.jpowsour.2017.08.067.

[33] A. Morin, G. Gebel, L. Porcar, Z. Peng, N. Martinez, A. Guillermo, S. Lyonnard, Quantitative Multi-Scale Operando Diagnosis of Water Localization inside a Fuel Cell, J. Electrochem. Soc. 164 (2017) F9–F21. https://doi.org/10.1149/2.1401614jes.

[34] J. Biesdorf, A. Forner-Cuenca, T.J. Schmidt, P. Boillat, Impact of Hydrophobic Coating on Mass Transport Losses in PEFCs, J. Electrochem. Soc. 162 (2015) F1243. https://doi.org/10.1149/2.0861510jes.

[35] E. Stavropoulou, E. Andò, A. Tengattini, M. Briffaut, F. Dufour, D. Atkins, G. Armand, Liquid water uptake in unconfined Callovo Oxfordian clay-rock studied with neutron and X-ray imaging, Acta Geotech. (2018). https://doi.org/10.1007/s11440-018-0639-4.

[36] S. Chevalier, N. Ge, M.G. George, J. Lee, R. Banerjee, H. Liu, P. Shrestha, D. Muirhead, J. Hinebaugh, Y. Tabuchi, T. Kotaka, A. Bazylak, Synchrotron X-ray Radiography as a Highly Precise and Accurate Method for Measuring the Spatial Distribution of Liquid Water in Operating Polymer Electrolyte Membrane Fuel Cells, J. Electrochem. Soc. 164 (2017) F107–F114. https://doi.org/10.1149/2.0041702jes.

[37] T.A. Zawodzinski, M. Neeman, L.O. Sillerud, S. Gottesfeld, Determination of water diffusion coefficients in perfluorosulfonate ionomeric membranes, J. Phys. Chem. 95 (1991) 6040–6044. https://doi.org/10.1021/j100168a060.

[38] D.S. Hussey, D. Spernjak, A.Z. Weber, R. Mukundan, J. Fairweather, E.L. Brosha, J. Davey, J.S. Spendelow, D.L. Jacobson, R.L. Borup, Accurate measurement of the through-plane water content of proton-exchange membranes using neutron radiography, J. Appl. Phys. 112 (2012) 104906. https://doi.org/10.1063/1.4767118.

[39] K.C. Neyerlin, H.A. Gasteiger, C.K. Mittelsteadt, J. Jorne, W. Gu, Effect of Relative Humidity on Oxygen Reduction Kinetics in a PEMFC, J. Electrochem. Soc. 152 (2005) A1073–A1080. https://doi.org/10.1149/1.1897368.

[40] Y.B. Kim, Study on the effect of humidity and stoichiometry on the water saturation of PEM fuel cells, Int. J. Energy Res. 36 (2012) 509–522. https://doi.org/10.1002/er.1845.

[41] D. Muirhead, R. Banerjee, J. Lee, M.G. George, N. Ge, H. Liu, S. Chevalier, J. Hinebaugh, K. Han, A. Bazylak, Simultaneous characterization of oxygen transport resistance and spatially resolved liquid water saturation at high-current density of polymer electrolyte membrane fuel cells with varied cathode relative humidity, Int. J. Hydrog. Energy. 42 (2017) 29472–29483. https://doi.org/10.1016/j.ijhydene.2017.10.031.

[42] Y. Tabuchi, T. Shiomi, O. Aoki, N. Kubo, K. Shinohara, Effects of heat and water transport on the performance of polymer electrolyte membrane fuel cell under high current density operation, Electrochimica Acta. 56 (2010) 352–360. https://doi.org/10.1016/j.electacta.2010.08.070.

[43] J. Lee, R. Yip, P. Antonacci, N. Ge, T. Kotaka, Y. Tabuchi, A. Bazylak, Impact of MPL Thickness on Water Management of PEMFC by Synchrotron X-ray Radiography, ECS Trans. 61 (2014) 69. https://doi.org/10.1149/06112.0069ecst.

[44] P. Oberholzer, P. Boillat, Local Characterization of PEFCs by Differential Cells: Systematic Variations of Current and Asymmetric Relative Humidity, J. Electrochem. Soc. 161 (2013) F139. https://doi.org/10.1149/2.080401jes.

[45] S. Chevalier, N. Ge, J. Lee, M.G. George, H. Liu, P. Shrestha, D. Muirhead, N. Lavielle, B.D. Hatton, A. Bazylak, Novel electrospun gas diffusion layers for polymer electrolyte membrane fuel cells: Part II. In operando synchrotron imaging for microscale

liquid water transport characterization, J. Power Sources. 352 (2017) 281–290. https://doi.org/10.1016/j.jpowsour.2017.01.114.

[46] N. Ge, R. Banerjee, D. Muirhead, J. Lee, H. Liu, P. Shrestha, A.K.C. Wong, J. Jankovic, M. Tam, D. Susac, J. Stumper, A. Bazylak, Membrane dehydration with increasing current density at high inlet gas relative humidity in polymer electrolyte membrane fuel cells, J. Power Sources. 422 (2019) 163–174. https://doi.org/10.1016/j.jpowsour.2019.03.001.

[47] M. Lopez-Haro, L. Guétaz, T. Printemps, A. Morin, S. Escribano, P.-H. Jouneau, P. Bayle-Guillemaud, F. Chandezon, G. Gebel, Three-dimensional analysis of Nafion layers in fuel cell electrodes, Nat. Commun. 5 (2014) 5229. https://doi.org/10.1038/ncomms6229.

[48] J. Peron, Z. Shi, S. Holdcroft, Hydrocarbon proton conducting polymers for fuel cell catalyst layers, Energy Environ. Sci. 4 (2011) 1575–1591. https://doi.org/10.1039/C0EE00638F.

[49] S. Holdcroft, Fuel Cell Catalyst Layers: A Polymer Science Perspective, Chem. Mater. 26 (2014) 381–393. https://doi.org/10.1021/cm401445h.

[50] Q. Meyer, N. Mansor, F. Iacoviello, P.L. Cullen, R. Jervis, D. Finegan, C. Tan, J. Bailey, P.R. Shearing, D.J.L. Brett, Investigation of Hot Pressed Polymer Electrolyte Fuel Cell Assemblies via X-ray Computed Tomography, Electrochimica Acta. 242 (2017) 125–136. https://doi.org/10.1016/j.electacta.2017.05.028.